Article

Design and Optimization of Geometry of Liquid Feed Conveyor Pipes

Yuwen Xia [1,2], Jie Hu [1,2], Huiyue Hu [1,2], Haibin Hu [1,2], Jiajia Xiao [3] and Renxin Liu [1,2,*]

1   School of Engineering, Jiangxi Agricultural University, Nanchang 330045, China;
    xiayuwen@stu.jxau.edu.cn (Y.X.); hujie9@jxau.edu.cn (J.H.); huiyuehu@stu.jxau.edu.cn (H.H.);
    1750820083@stu.jxau.edu.cn (H.H.)
2   Research Center of Animal Husbandry Facility Technology Exploitation, Nanchang 330045, China
3   Jiangxi Zengxin Technology Co., Ltd., Xinyu 338000, China; xinxiaojiaj@jxxyzxkj.com
*   Correspondence: liurenxin1@jxau.edu.cn

Abstract: The promotion and use of liquid feeding face the challenge of insufficiently stable delivery. This issue can be resolved, in part, by using the spiral flow produced by a spiral pipe (SPP). The aim of this study is to investigate how the structural characteristics of the spiral pipe affect the flow state of the liquid feed, and for this purpose, the computational fluid dynamics (CFD) technique has been employed and the liquid feed delivery process has been simulated by means of an Eulerian two-fluid model The results reveal a significant improvement in the slurry's homogeneity as it traveled through a spiral pipe compared with a straight pipe (STP). The swirl number normally increased with the number, length, height, and angle of the spiral pipe's guide vanes. The solid-phase distribution was more homogeneous when values of $N = 1$, $L = 1D$, $H = 3/8R$, and $\theta = 20°$ were used, respectively, and the *COV* within 10D downstream of the outlet of the spiral pipe was 3.902% smaller than that of the straight pipe. The results of this study can be used as a reference for the design of liquid feed-conveying pipes.

Keywords: solid–liquid flow; swirl number; swirl-inducing pipe; CFD; liquid feeds; structural optimization

1. Introduction

Liquid feeds, which are fluid mixtures of water and feed mixed in specific proportions, offer numerous advantages over traditional solid dry feeds [1]. These advantages include an improved pigsty environment [2], reduced feed costs [3], the reduced use of antibiotics [4,5], the assisted weaning of piglets [6], improved palatability, and enhanced gut health [7,8]. As a result, liquid feeds offer the potential for a wide range of uses in pig farming. However, the process of liquid feeding is complex, and with recent increases in labor expenses, current breeding companies frequently use liquid feed systems as the carriers of liquid feeding. A liquid feed system consists of four components: a storage unit, a mixing unit, a dispensing unit, and an automatic control system. Dry feed is combined with water and pumped to the trough via pipes and throttling devices. Liquid feed systems have a high level of automation; however, it must be recognized that the upfront investment cost of these systems is high, and farmers adopting these systems require sufficient start-up capital, which is more feasible for pig farms with a larger scale of operation. Large-scale hog-farming enterprises usually have larger inventories, and a single pipeline is usually responsible for a sufficient amount of feed supply for several pens, which can be up to several hundred meters in length. Liquid feed is a two-phase flow consisting of solids and liquids with significantly different specific gravities. Feed stratification issues frequently arise during long-distance transport, resulting in an unequal nutrient distribution in various downstream ports, which impairs the neatness of hog slaughter. In more severe circumstances, this might lead to the obstruction of the conveying pipeline, resulting in economic losses. Therefore, it is

particularly important to prevent liquid feed from stratifying during transportation [9] and to maintain the homogeneity and stability of liquid feed.

Particles in a flow field are not necessarily evenly dispersed due to the effects of gravity, buoyancy, and drag forces. Based on the particle concentration distribution in a flow field, Newitt et al. [10] classified two-phase solid–liquid flow into four flow patterns: homogeneous flow, heterogeneous flow, moving beds, and stationary beds.

Homogeneous flow: At this point, the feed particles are evenly dispersed in the flow field and fully suspended.

Heterogeneous flow: The lower section of the pipe has a significantly higher solid-phase concentration than the upper section, but no solid-phase deposition can be observed.

Moving bed: The solid-phase particles initially gather at the pipe's bottom and progress forward through a sliding or jumping motion.

Stationary bed: On the base of the moving bed, particles continue to aggregate and stop moving. The flow area in the pipe is reduced, and there is a risk of clogging the pipe.

To avoid the appearance of moving and stationary beds, which reduces the likelihood of deposits from liquid feed, the velocity of feed conveying can be increased to exceed the critical velocity in order to transform the moving bed into a heterogeneous flow and optimize the distribution uniformity of feed particles in the liquid feed [11].

The definition of critical velocity is now a topic of debate in the academic community. For solid–liquid two-phase flow, Thomas, Durand, and Graf used the "minimum transport velocity", "limit deposit velocity", and "critical deposit velocity" as the critical velocity, respectively [12]. Scholars' definitions of the critical velocity of flow make it evident that raising the conveying velocity can enhance the homogeneity of liquid feed. However, high flow rates also lead to increased pipe wear [13], and the loss of conveying resistance in the two-phase pipe is proportionate to the square of the velocity [14]. Therefore, it is not the most cost-effective option to only increase the carrying speed.

Spiral flow, a unique flow phenomenon known for its strong carrying capacity, is created when axial flat flow and circumferential spinning flow combine. It is currently one of the strategies used most frequently to deal with stability problems in solid–liquid flow with two phases [15]. The enhanced homogeneity of two-phase fluids carried via spiral flow has been the subject of numerous investigations [16–18]. Compared with traditional circular pipes, spiral pipes have a lower critical velocity of flow for the same slurry [19]. Yanuar et al. [20] investigated solid–liquid two-phase flow via spiral pipes at various angles. The study found that employing spiral pipes improved the homogeneity of a coal slurry by 22%, while also reducing the conveying resistance by around 30%. Internal spiral ribs in pipelines lower the pressure gradients and power consumption for the low-velocity transport of solid materials, according to research by Charles et al. [21]. For moving settling slurries, ribbed pipes with a particular pitch-to-diameter ratio are more energy-efficient than smooth pipes. Li et al. [22] carried out in-depth experimental research and presented a spiral flow pneumatic conveying system. Their findings showed that the spiral flow pneumatic conveying system achieved optimized outcomes in terms of the pressure drop, pipe wall wear, and critical flow velocity when compared with axial flow pneumatic conveyance. Fokeer et al. [23] discovered that the Reynolds stress model (RSM) can properly represent eddy currents in a three-bladed spiral pipe, while the usual k-ε model is not relevant. Furthermore, while simulating gas-phase flow, the problems posed by a highly anisotropic turbulent flow must be considered, and the credibility, mistakes, and uncertainties of computational simulations must be examined during the validation and verification procedures. Zhou et al. [24] used a CFD-DEM model to investigate the pneumatic conveyance efficiency of three different types of vortex-generating pipes: internal helical-blade, rifle, and three-blade pipes. For the initial conveyance, the three-blade pipe was the most efficient and had the lowest total pressure at the inlet. The internal helical pipe, however, demonstrated the best efficiency for steady conveyance. It achieved about 26% energy efficiency at velocities below 40 m/s, which makes it perfect for steady transport in coarse-particle vortex flow systems. Ariyaratne [25] created and improved the

transition pipe for a leaf helix. The redesigned transition pipe minimizes the pressure loss and vortex attenuation while enhancing the induced vortex rate.

In conclusion, spiral flow is clearly economically valuable when it comes to pipeline transportation. Tangential intake flow [17], spiral pipe installation [18,24,26], and pipe rotation are examples of the traditional generating techniques for spiral flow. Among them, a spiral pipe is the research object of this study because of its simple structure and low cost of use. The features of the spiral flow that a spiral pipe generates may vary depending on the pipe's structural alterations. Due to the high expense and complexity of experimental studies, numerical simulations are popular tools for studying solid–liquid two-phase flows. In this study, the Eulerian–Eulerian approach was utilized to simulate the flow process of liquid feed in a spiral pipe, and the transport model's reliability was validated using Schaan et al.'s experimental data [27]. Based on the simulation results, this study examined the impact of a spiral pipe's structural characteristics on the flow state of liquid feed. Using the swirl number generated per unit additional pressure drop as an evaluation index of the spiral pipe, the optimal combination of the structural parameters of the spiral pipe was obtained to achieve a low energy consumption and the long-distance transportation of liquid feed.

2. Materials and Methods

2.1. Simulation Modeling

This study examined a spiral pipe with guide vanes. The guiding vane comprised a 2 mm thick plate that was twisted and placed perpendicular to the pipe wall. Figure 1a depicts a schematic diagram of the spiral pipes. Figure 1b shows a plan view of the pipe inlet. To examine the difference in the flow state of liquid feed in a spiral pipe and a straight pipe, simulation calculations for the flow state of the liquid feed in the straight pipe were also performed. The sole difference between the straight pipe and the spiral pipe was the absence of guiding vanes; the other dimensions, such as the length and the inner diameter, were identical. The structural differences between spiral pipes are determined by the number of guide vanes (N), the angle of the guide vane (θ), the length of the guide vane (L), and the height of the guide vane (H). Table 1 shows each of the structural properties of different spiral pipes. The geometric model of the simulation is shown in Figure 2.

(**a**)   (**b**)
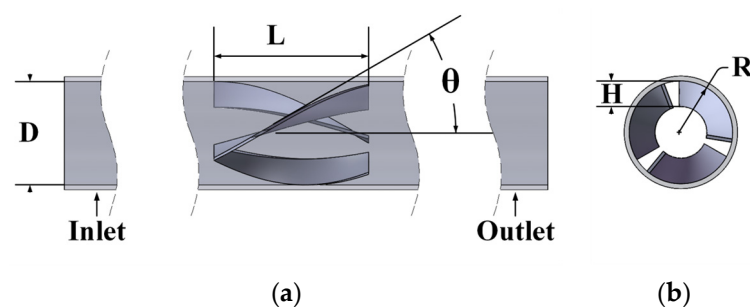
Figure 1. Schematic of spiral pipes with guide vane: (**a**) side view of spiral pipes; (**b**) inlet plan of spiral pipes.

In this research, water and feed particles were numerically calculated using the Fluent software version 2022R1. The Euler–Euler model was used, and the phase-coupled SIMPLE algorithm was used for velocity and pressure coupling. In the Fluent software, the precision of discretization schemes greatly impacts the computational results. Currently, Fluent provides four pressure interpolation schemes: standard, PRESTO, second-order, and body force-weighted. Given the significant pressure fluctuations in the spiral pipe and the focus on pressure loss as the evaluation metric for the spiral pipe, the high-precision second-order upwind scheme was selected for the pressure interpolation. For the momentum, volume, turbulent kinetic energy, and turbulent dissipation rate, Fluent also provides first-order upwind and second-order upwind schemes for spatial discretization. Considering that

most grids in this study were structured and aligned with the flow direction, they suited the first-order upwind scheme well. This scheme is advantageous for structured grids, offering quick computation, straightforward convergence, and improved stability. Therefore, the first-order upwind scheme was chosen for the spatial discretization of the momentum, volume, turbulent kinetic energy, and turbulent dissipation rate in this research. The calculation was considered to have reached convergence when all the residual values were less than 10^{-4}. The parameters are provided in Table 2.

Table 1. Specific structural parameters of different spiral pipes.

Number (N)	Angle (θ)	Length (L)	Height (H)	Code
1	30°	1.5D	0.5R	N1
2	30°	1.5D	0.5R	N2
3	30°	1.5D	0.5R	N3
4	30°	1.5D	0.5R	N4
5	30°	1.5D	0.5R	N5
6	30°	1.5D	0.5R	N6
3	10°	1.5D	0.5R	A1
3	20°	1.5D	0.5R	A2
3	40°	1.5D	0.5R	A4
3	50°	1.5D	0.5R	A5
3	60°	1.5D	0.5R	A6
3	30°	0.5D	0.5R	L1
3	30°	1.0D	0.5R	L2
3	30°	2.0D	0.5R	L4
3	30°	2.5D	0.5R	L5
3	30°	3.0D	0.5R	L6
3	30°	1.5D	0.125R	H1
3	30°	1.5D	0.25R	H2
3	30°	1.5D	0.375R	H3
3	30°	1.5D	0.625R	H5
3	30°	1.5D	0.75R	H6
3	30°	1.5D	0.875R	H7
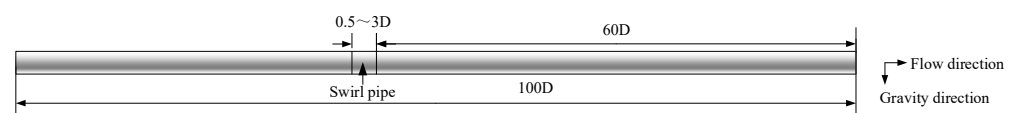
Figure 2. Schematic representation of pipeline test sections.

Table 2. Simulation parameters.

Object	Settings	Parameters
Liquid phase	Density/(kg·m^{-3})	998.2
	Viscosity/(kg·m^{-1}·s^{-1})	1.003×10^{-3}
Solid phase	Density/(kg·m^{-3})	1500
	Volume fraction	0.175
	Diameter/(μm)	75
Inlet	Velocity inlet/(m·s^{-1})	3
Outlet	Pressure outlet/(Pa)	0
Wall	No-slip condition	
Turbulence	Turbulence intensity/(%)	3.50399
	Hydraulic diameter/(m)	0.063

2.2. Governing Equation of the Liquid and Solid Phases

The currently available numerical approaches for solid–liquid dual-phase flow calculations are the Euler–Lagrange technique [28] and the Euler–Euler technique [29]. The Euler–Lagrange approach employs the Navier–Stokes (N-S) equations to solve the carrier fluid directly, treating it as a continuous phase. In order to ascertain the trajectory of the particle phase, the particles are regarded as a discrete phase and incorporated into the Lagrange coordinate system. Due to computational and statistical limitations, the Euler–Lagrange approach is not fully applicable to this topic, especially when working with small particles and high-concentration solid–liquid systems. The Euler–Euler technique views liquid and solid phases as continuous phases that mix and coexist at every point in the flow field. Every phase has its own temperature, volume fraction, and velocity. This work simulated and solved the two-phase flow of solids and liquid in a helical pipe using the Euler–Euler technique in conjunction with the RNG k-ε turbulence model [30–32].

The flow of liquid feed within the pipeline adhered to the continuity equation and momentum conservation equation.

The continuity equation is as follows [33]:

$$\frac{\partial \alpha_i \rho_i}{\partial t} + \nabla(\alpha_i \rho_i u_i) = 0 \tag{1}$$

where α is the volume fraction of a particular phase, ρ is the density of a particular phase, t is the time, and u is the velocity of a particular phase.

The momentum equations are as follows [34]:

$$\frac{\partial}{\partial t}(\alpha_l \rho_l u_l) + \nabla \cdot (\alpha_l \rho_l u_l u_l) = -\alpha_l \nabla p + \nabla \cdot \tau + \alpha_l \rho_l g + F_{s,l} \tag{2}$$

$$\frac{\partial}{\partial t}(\alpha_s \rho_s u_s) + \nabla \cdot (\alpha_s \rho_s u_s u_s) = -\alpha_s \nabla p + \nabla \tau + \alpha_s \rho_s g + F_{l,s} \tag{3}$$

where α_l and α_s are the liquid-phase volume fraction and solid-phase volume fraction, u_l and u_s are the velocities of the liquid and solid phases, ρ_l and ρ_s are the densities of the liquid and solid phases, p is the two-phase shared pressure, and $\nabla \tau$ is the stress–strain tensor.

In 1986, Yakhot and Orszag et al. [35] applied the renormalization group (RNG) theory to turbulent flows with high Reynolds numbers, resulting in the RNG k-e model. The RNG k-ε model can accurately simulate issues such as separated flow, secondary flow, and spiral flow [36]. Pathak [37] used the RNG k-e model to simulate a slurry, and the numerical results he obtained were consistent with the experimental data from the horizontal pipe, demonstrating the model's validity. The fundamental equation is as follows:

$$\frac{\partial(\rho k)}{\partial t} + \frac{\partial(\rho k u_i)}{\partial x_i} = \frac{\partial}{\partial x_j}\left[\alpha_k(\mu + \mu_t)\frac{\partial k}{\partial x_j}\right] + G_k - \rho\varepsilon + S_k \tag{4}$$

$$\frac{\partial(\rho\varepsilon)}{\partial t} + \frac{\partial(\rho\varepsilon u_i)}{\partial x_i} = \frac{\partial}{\partial x_j}\left[\alpha_\varepsilon(\mu + \mu_t)\frac{\partial\varepsilon}{\partial x_j}\right] + C_{1\varepsilon}G_k\frac{\varepsilon}{k} - C_{2\varepsilon}\rho\frac{\varepsilon^2}{k} - R_\varepsilon + S_\varepsilon \tag{5}$$

where t is the time, ρ is the density of the fluid, μ_t is the turbulent viscosity, u_i is the velocity vector, x_i and x_j are the coordinate components, G_k is the turbulent kinetic energy production term, ε is the turbulent kinetic energy dissipation rate, k is the turbulent kinetic energy, $C_{1\varepsilon} = 1.42$, $C_{2\varepsilon} = 1.68$, $\alpha_k = \alpha_\varepsilon = 1.393$, and S_k and S_ε are the user-defined source terms [38].

There are numerous drag force equations that concern solid–liquid two-phase flow, with the typical models including the Wenyu drag model and the Gidaspow drag model.

The expression for the Wenyu drag model [39] is as follows:

$$C_D = r_c^{-1.65} max \left(\frac{24}{Re'_p} \left(1 + 0.15 Re'^{0.687}_p \right), 0.44 \right) \tag{6}$$

$$Re'_p = r_c Re \tag{7}$$

The expression for the Gidaspow drag model [40] is as follows:

$$C_D = C_D(Wen\ Yu) \qquad r_c > 0.8 \tag{8}$$

$$c_{\alpha\beta}^{(d)} = 150 \frac{(1 - r_c)^2 \mu_c}{r_c d_p^2} + \frac{7}{4} \frac{(1 - r_c)\rho_c |U_c - U_d|}{d_p} \qquad r_c < 0.8 \tag{9}$$

where d_p is the particle diameter, and r_c is the volume fraction of the liquid phase. It can be observed from the relationship that for the low-concentration mixed fluid ($r_c > 0.8$) employed in the numerical calculations of this study, the use of the Wenyu drag model to obtain a description was more appropriate.

2.3. Model Validation

2.3.1. Grid Size Independence Tests

The test pipe was meshed using Fluent Meshing software version 2022R1 as shown in Figure 3. To better adapt to the complex geometry of the pipe and ensure the boundary layer and flow field changes were accurately captured in the simulation, an unstructured mesh was employed at the boundary. Meanwhile, within the interior of the fluid domain, a hexahedral structured mesh was utilized. This structured mesh exhibited better regularity and contributed to improving the efficiency of the numerical computation. This combined meshing strategy carefully balanced the requirement for the accurate modeling of complex geometries and the overall structure of the fluid domain while maintaining computational efficiency.

(a)

(b)

(c)
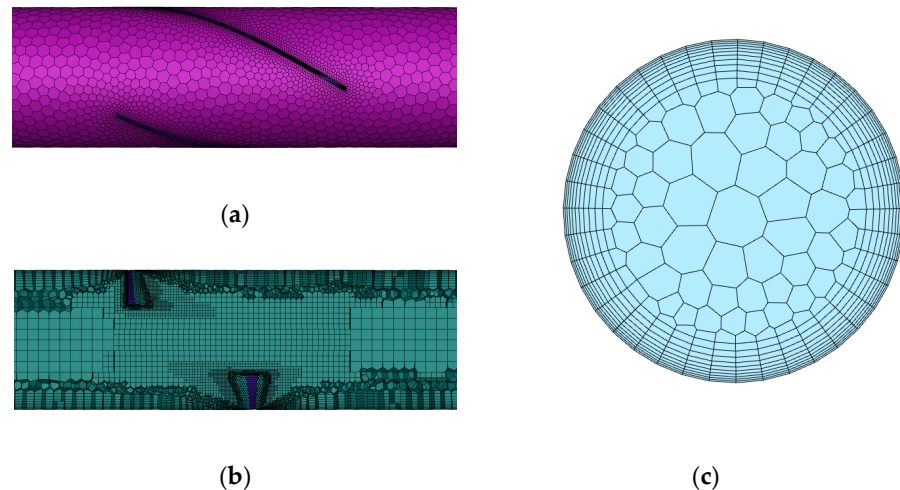
Figure 3. Grid division diagram: (**a**) wall grid; (**b**) internal grid; and (**c**) inlet/outlet grid.

To effectively reduce the computational burden of this model, we adopted six meshes with different numbers of nodes (range: 169,768~38,602,658) as shown in Table 3, while ensuring that the boundary layer y+ was less than 30. We verified the mesh independence with the pressure drop downstream of the spiral pipes. The relevant computational results are displayed in Figure 4 below. By observing the relationship between the degree of the pressure drop trend and the number of nodes, we concluded that after the number of nodes exceeds 3,034,836, the influence of increasing the number of meshes on the pressure drop becomes insignificant. Therefore, to ensure computational efficiency while maintaining the

reliability of the results, we finally chose a grid with a node number of about 3,034,836 for the simulation.

Table 3. Grid parameters.

Grid	Number of Nodes	Number of Cells
Coarse grid	169,768	60,274
Coarse-M grid	580,940	186,099
Medium grid	1,308,650	467,189
Medium-M grid	3,034,836	1,126,833
Fine-M grid	10,651,510	4,042,539
Fine grid	38,602,658	14,861,850
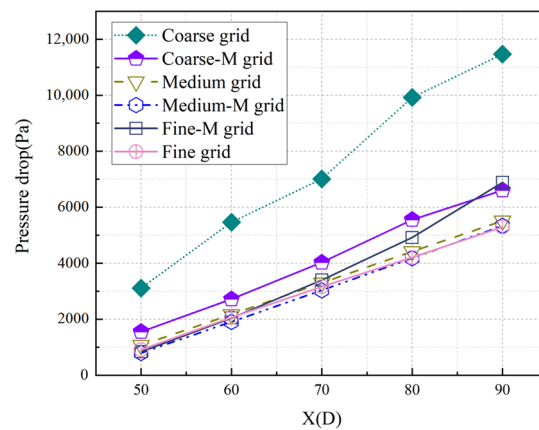
Figure 4. Pressure drops from each cross-section of the test pipe to the outlet cross-section of the spiral pipe (40D) at different grid scales.

2.3.2. Experimental Verification

Many researchers have experimented with the concentration distribution of solid–liquid two-phase flow throughout the last few decades. In this study, the numerical simulation conditions were the same as the experimental conditions of Schaan et al. The simulation was performed on a circular pipe with an inner diameter of 150 mm, a slurry particle size of 0.09 mm, concentrations of 15% and 32%, and flow speeds of 1.4 m/s, 1.5 m/s, and 3 m/s. The numerical calculations were then compared with the experimental results. Figure 5 shows the average difference between the estimated and experimental results under three distinct working conditions: 12.07%, 14.40%, and 5.10%. The differences between the experimental and numerical simulation results were all less than 15% and were, therefore, within the acceptable range [41]; hence, the present numerical simulation approach was deemed relatively trustworthy.
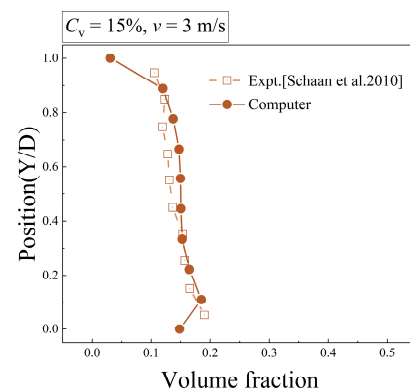
Figure 5. *Cont.*
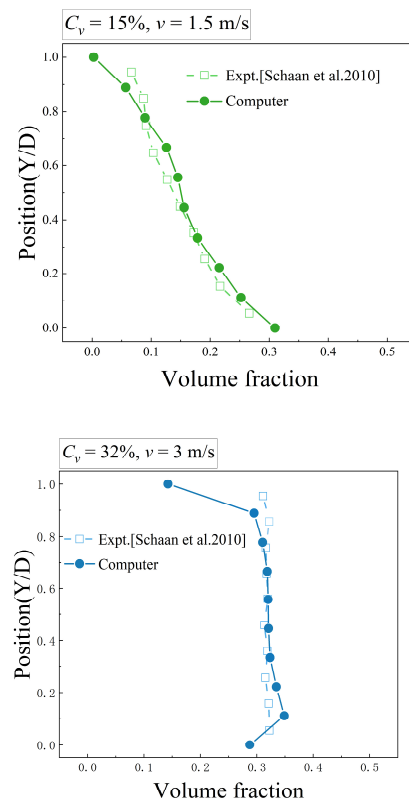
Figure 5. The calculated volume fraction distributions were compared with the experimental results [27].

3. Results

3.1. Velocity Distributions

Figure 6 shows the axial velocity contour graphs for the spiral and straight pipes at various cross-sections. As seen in the images, the insertion of the spiral pipe significantly altered the distribution of velocity in the initial flow field, lowering the zone of flow in the piping and resulting in a large rise in velocity at the pipe's center. Simultaneously, the existence of a low-pressure zone on the leeward edge of the guide vanes caused the high-velocity region to extend to the backside of the guide vanes, resulting in a distinct wake. While the flow field developed, the tangential velocities dropped as the fluid flowed through the spiral pipe, and the high-velocity zones gradually returned to the center of the pipe, and the velocity distributions of the straight and spiral pipes gradually became similar.

In order to comprehend the circumferential velocity more fully, the swirl number [22] notion is presented. The equation below defines the swirl number as the proportion of the fluid's radial angular velocity to its axial velocity:

$$S = \frac{\int_0^R uwr^2 dr}{R \int_0^R u^2 r dr} \tag{10}$$

where u and w are the axial and tangential velocities, and R is the pipe radius.

Figure 7 depicts the swirl number downstream of the spiral pipe under various configurations. The figure shows that the swirl number at the downstream end of the spiral pipe progressively increased with the number of guide vanes and the guide vane length, height, and angle, and the rate of increase gradually decreased. This suggests that structural differences in spiral pipes have a significant impact on the swirling characteristics of the spiral flows they produce. The spiral flow produced by spiral pipes is mostly due to the distinctive spiral form of the pipes. As the fluid flows through the spiral pipes, it

strikes the windward side of the guide vanes, causing the guide vanes' reaction force to impose a moment on the fluid, resulting in tangential flow. To some extent, increasing the length, number, height, and angle of the guiding vanes will increase the amplitude and duration of this moment.
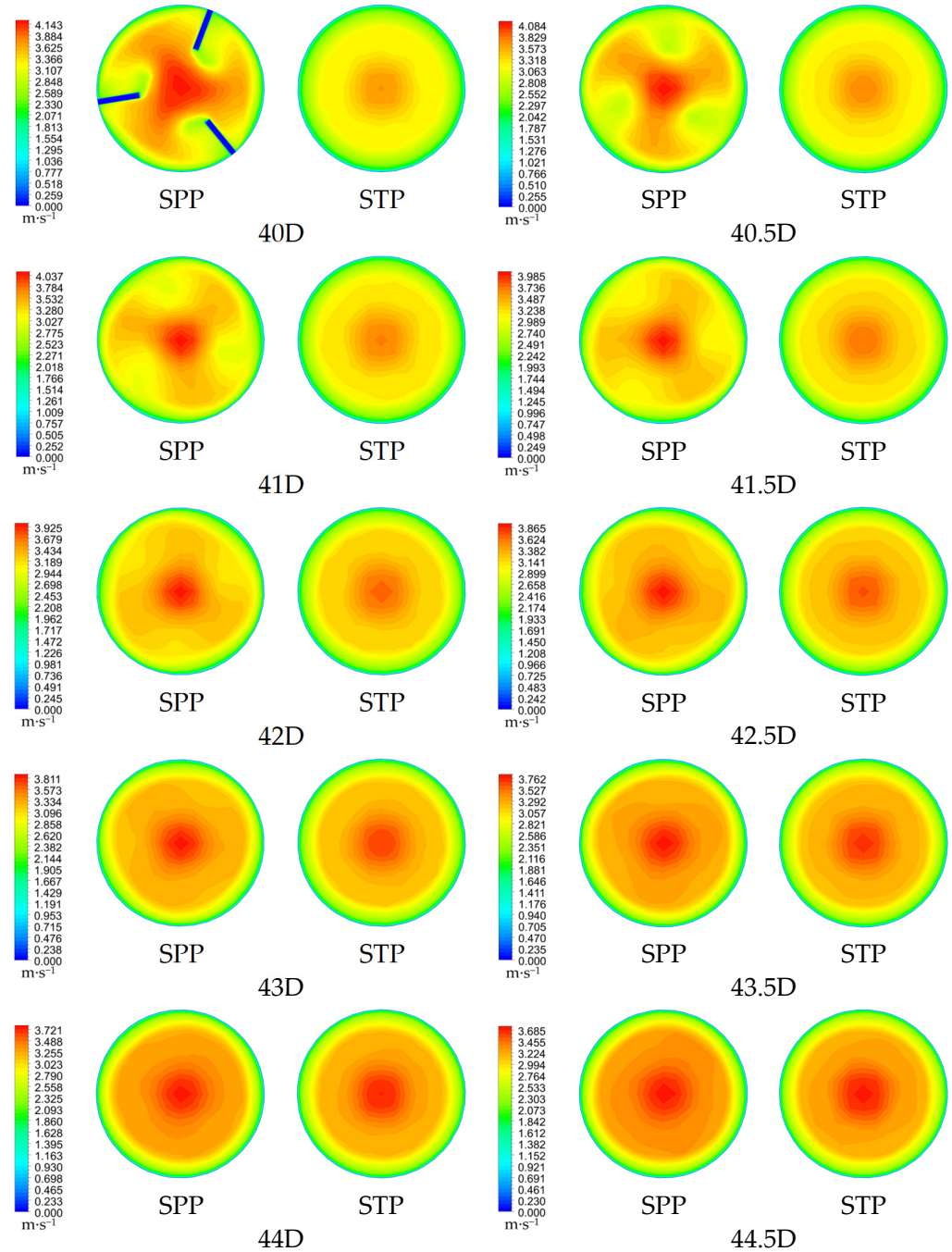
Figure 6. Comparison of velocity distributions in spiral pipes (N3) vs. straight pipes.

Modifying the number, length, height, and angle of the guide vanes in the construction of spiral pipes allows for the effective control of the swirl intensity downstream of the spiral pipe, which serves as a significant reference for optimizing the design of spiral pipes.

The angle of the guide vanes

The number of guide vanes

The height of the guide vanes

The length of the guide vanes
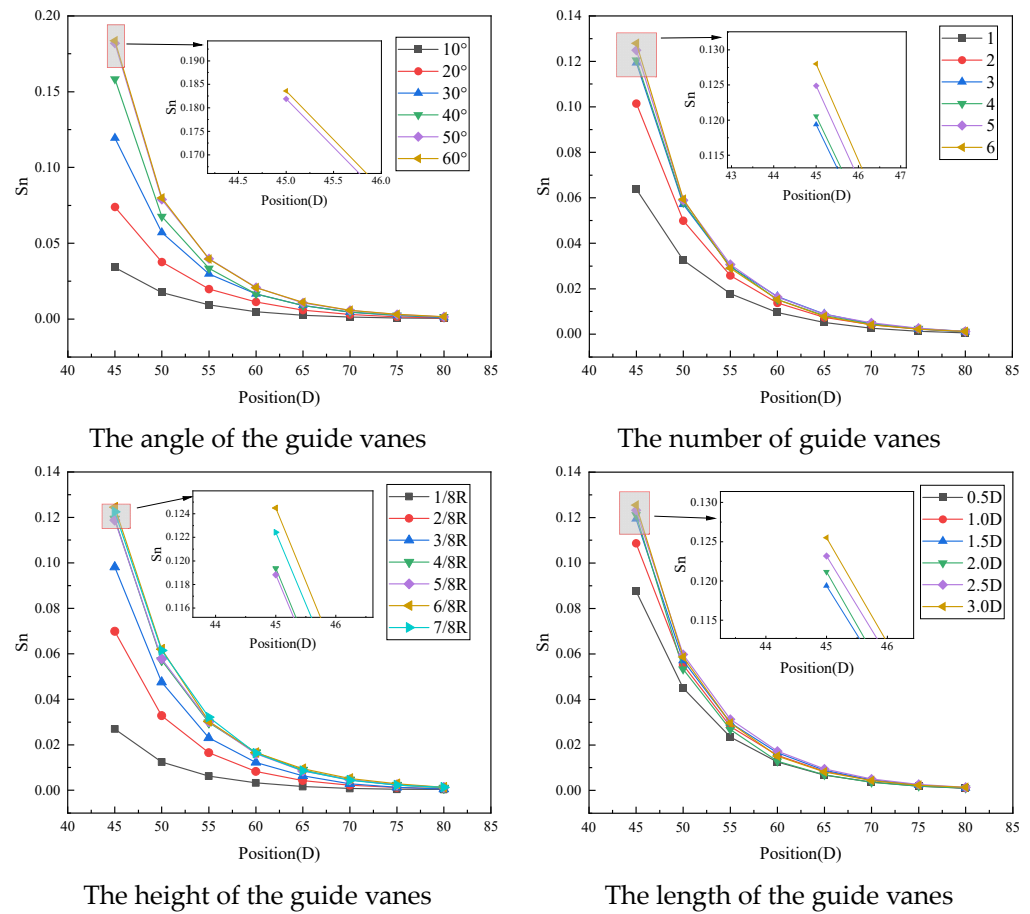
Figure 7. Axial variation in swirl number for different spiral pipes.

3.2. Swirl Effectiveness

Within the scope of the simulation experiments investigated in this study, the generation of spiral flow was always accompanied by the appearance of additional pressure drops. To better judge the spiral flow generation efficiency of different spiral pipes, the performance evaluation index S_e (swirl effectiveness) of spiral pipes was introduced. S_e represents the number of swirls induced per unit of additional pressure drop, and the definition equation is as follows:

$$S_e = \frac{S_n}{\Delta P_i - \Delta P} \tag{11}$$

where S_n is the swirl number at cross-section B, ΔP_i (kPa) is the pressure drop between sections A and B in the spiral pipe, and ΔP (kPa) is the pressure drop between sections A and B in a straight pipe. The locations of sections A and B are shown in Figure 8.
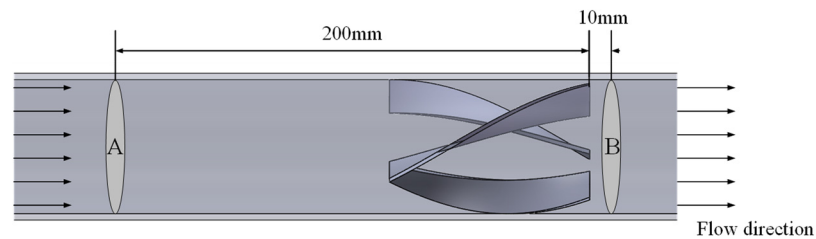
Figure 8. Schematic of the locations of cross-sections A and B.

Figure 9 depicts the influence of a spiral pipe's structural factors on the S_e. As shown in the image, the S_e was negatively correlated with the number of guide vanes, and the pro-

duced spiral flow rate reached its greatest level when the number of guide vanes was $N = 1$. This result indicates that the design of a single guide vane is highly effective in improving the operating performance of spiral pipes. The S_e tended to rise and subsequently drop with a rise in the length (L), height (H), or angle (θ) of the guide vane. The maximum value was achieved at around $L = 1D$, $H = 3/8R$, and $\theta = 20°$. In Figure 7, it can be seen that the Sn increased with the increase in the N, L, H, and θ, and the growth rate gradually slowed down. The additional pressure loss mainly came from the friction and collision between the fluid and the guide vane, which did not slow down the growth rate due to the increase in the N, L, H, and θ. Therefore, when the N, L, H, and θ exceeded a certain threshold, the S_e decreased with the increase in the N, L, H, and θ. The result is that $N = 1$, $L = 1D$, $H = 3/8R$, and $\theta = 20°$ became the better solution in the univariate analysis. Except for the number of guide vanes, the length, height, and angle of the guide vanes were continuous within the range of values, and by using S_e as the dependent variable and L, H, and R as the independent variables, the maximum value of S_e could be obtained at around $L = 1D$, $H = 3/8R$, and $\theta = 20°$, which further optimized the efficiency of the helical pipe to obtain a larger number of swirls with a smaller additional pressure loss.
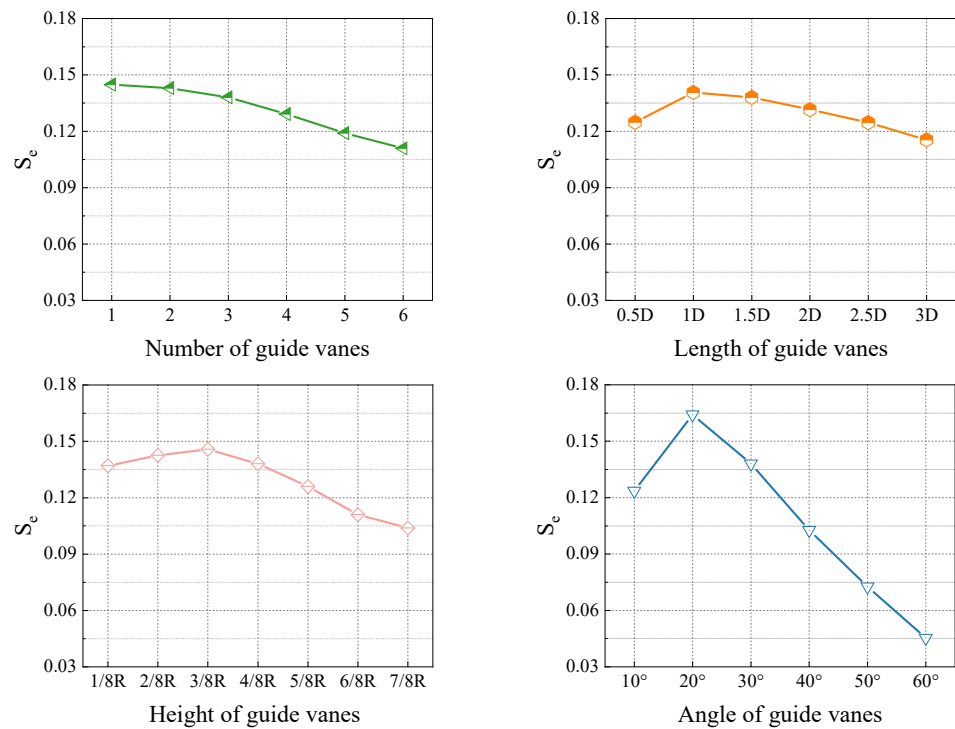
Figure 9. Influence of spiral pipe structure on swirl effectiveness.

3.3. Concentration Distributions

Figure 10 illustrates the solid-phase particle distributions of helical pipes A1, A2, N3, A4, A5, and A6 in their tangential planes (at distances ranging from 40D to 70D), which are structurally detailed and parameterized in Table 1. As shown in the figure, a strong spiral flow caused solid-phase material to accumulate on the pipe wall. This indicates a significant role played by the helical flow in the distribution of particles. A strong spiral flow, with its prominent centrifugal force and wall shear effects, did not cause consolidation, even though the solid component's concentration was higher near the pipe wall.

While the flow field evolved, the spiral flow became less intense. At this point, the centrifugal force was no longer adequate to drive the particles toward the pipe wall. However, the upward velocity component of the helical flow still partially offsets the influence of gravity. Consequently, the sedimentation rate of particles slowed down, resulting in a more uniform distribution of the concentration in the flow field.
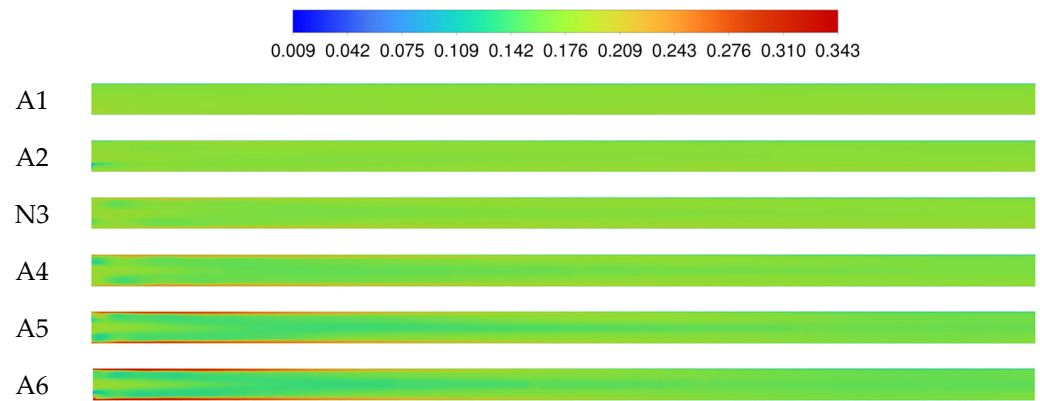
Figure 10. Distribution of concentrations downstream of different spiral pipes.

Between 40D and 90D of the test pipe, 250 cross-sections perpendicular to the axis were taken, with equal spacing between adjacent cross-sections. Sampling points were set in a square array format on each interface, with a spacing of approximately 0.707 mm between adjacent sampling points in the up, down, left, and right directions. The coefficient of variation (*COV*) of the solid-phase concentration was calculated for each cross-section using the sample sites' solid-phase concentrations. The smaller the value of the *COV*, the more homogeneous the solid-phase distribution on that cross-section. The *COV* was calculated as follows [42]:

$$COV = \frac{1}{\overline{x}} \sqrt{\frac{1}{n-1} \sum_{i=1}^{n} (x_i - \overline{x})^2}$$ (12)

where n is the number of sampling points in each cross-section, x_i is the concentration at a point on the cross-section, and $\overline{x}$ is the cross-sectional average concentration.

Figure 11 shows the distribution of the *COV* between 40D and 90D for the spiral pipe ($N = 1$, $L = 1D$, $H = 3/8R$, and $\theta = 20°$) and a straight pipe. As can be seen in the figure, the median and mean values of the *COV* for spiral pipes are smaller than those for straight pipes. This means that spiral pipes improve the homogeneity of a conveyed slurry. They can increase the pipeline conveying system's safety and increase the liquid feed's effective conveying distance.
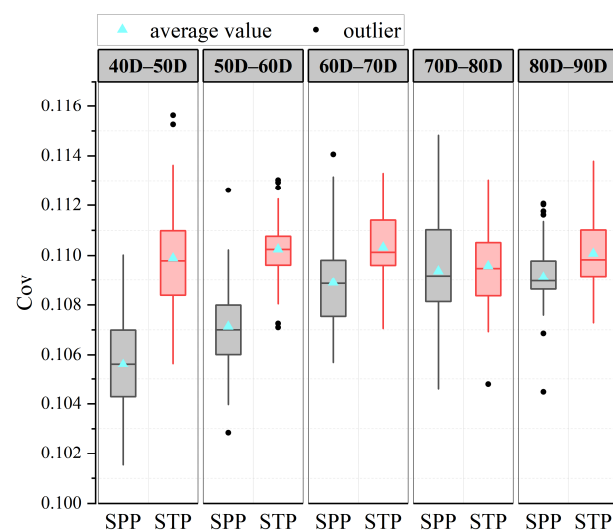
Figure 11. Box plot of uniformity for spiral pipes and straight pipes.

Up to this point, the liquid feeds mentioned in this text all had a velocity of 3 m/s at the inlet, corresponding to a Reynolds number of about 186,747. To explore the effect

of spiral pipes on the concentration distribution of liquid feeds under different Reynolds numbers, the Fluent software was used in this study to simulate the flow of liquid feeds inside a specific spiral pipe ($N = 1$, $L = 1D$, $H = 3/8R$, and $\theta = 20°$). The coefficient of variation (*COV*) was calculated for spiral pipes between 40D and 90D. The results are displayed in the box-and-line plots shown in Figure 12.
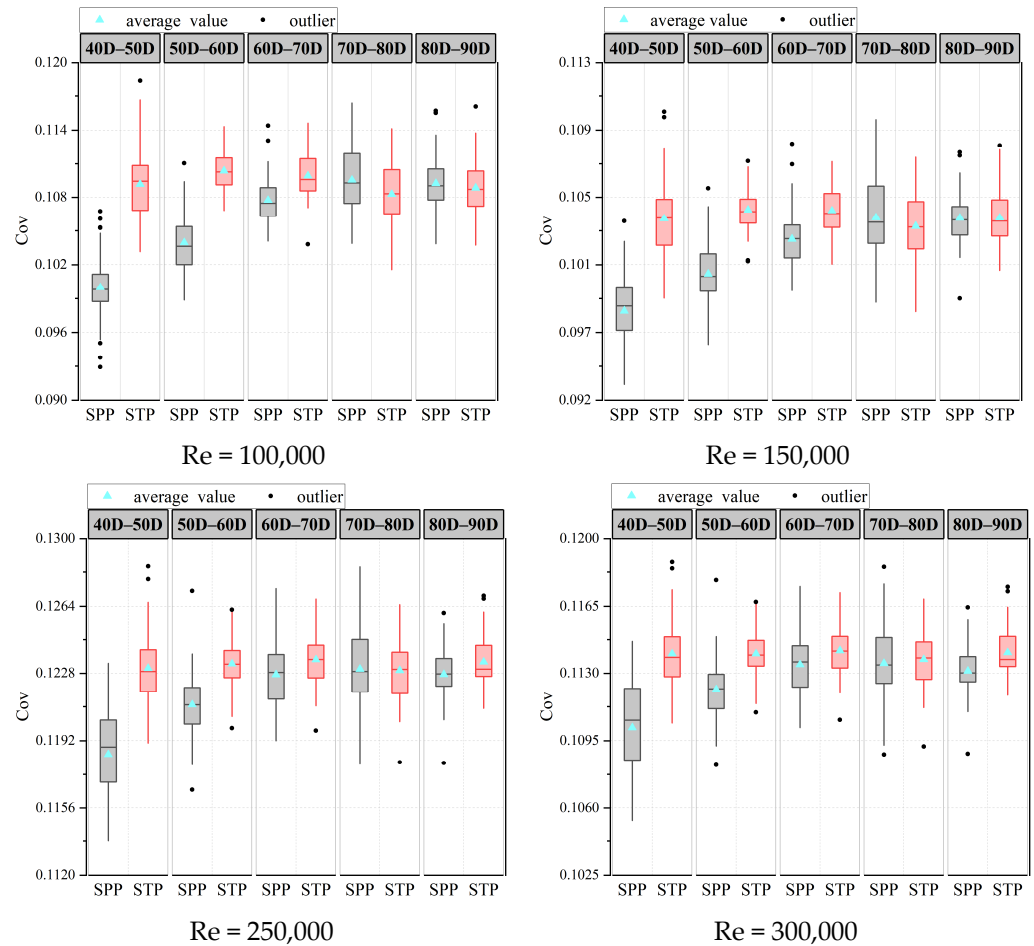
Figure 12. *COV* distributions of spiral pipe and straight pipe at different Reynolds numbers.

Figure 12 clearly demonstrates the effect of the choice of a spiral pipe on the downstream liquid feed uniformity enhancement under different Reynolds number conditions. In addition, by calculating the percentage reduction in the *COV* value of the spiral pipe relative to the straight pipe, the data in Table 4 specifically reveal the relative advantage of the spiral pipe in enhancing the uniformity of the liquid feed. From the analysis of the data in Table 4, it can be seen that the spiral pipe can indeed improve the uniformity of liquid feed within a certain range. However, the effectiveness of the spiral pipe in improving the uniformity of the liquid feed decreases as the conveying distance increases, instead making the liquid feed in the spiral pipe less uniform than in the straight pipe. This phenomenon may result from the rapid reduction in turbulent energy inside the spiral pipe and the gradual weakening of the spiral flow. Consider the portion of the downstream *COV* of the spiral pipe that has a lower *COV* than the *COV* of the straight pipe as the effective range of action of the spiral pipe. The length of this range is longer at high Reynolds numbers than at low Reynolds numbers. Under low-Reynolds number conditions, the spiral pipe is more effective in enhancing the uniformity of liquid feed and exhibits a greater reduction in *COV* values.

Table 4. Percentage reductions in *COV* values for spiral pipe versus straight pipe.

	40D–50D	50D–60D	60D–70D	70D–80D	80D–90D
Re = 1.5×10^5	8.416%	5.811%	1.982%	−1.175%	−0.374%
Re = 1.5×10^5	5.279%	3.644%	1.623%	−0.494%	0.008%
Re = 2.5×10^5	3.729%	1.791%	0.647%	−0.057%	0.541%
Re = 3.0×10^5	3.371%	1.635%	0.635%	0.176%	0.837%

4. Conclusions

To avoid the stratification and siltation of liquid feed in a conveying pipeline, this study designed and improved a spiral conveying pipe with a guide vane structure in a piggery. The flow field of the circular pipe with guide vanes was numerically simulated by the authors using the RNG k-e equation and the Eulerian two-fluid model. By analyzing the concentration distribution of the liquid feed in the pipe and the efficiency of the spiral pipe in inducing the generation of spiral flow, the following conclusions were drawn.

The fluid moving through the spiral pipe creates a spiral flow, which intensifies with the number, height, angle, and length of the guiding vanes. However, adding a spiral pipe increases the test pipe's overall pressure loss. Therefore, this study introduced the concept of S_e (swirl effectiveness), i.e., the number of swirls induced per unit of the additional pressure drop generated by the spiral pipes, to provide a quantitative index for the optimized design of spiral pipes. Under the simulated working conditions in this research, S_e achieved its maximum value when the number of guide vanes was $N = 1$, the length of the guide vanes was $L = 1D$, the height of the guide vanes was $H = 3/8R$, and the angle of the guide vanes was $\theta = 20°$. Under the same operating conditions, the average coefficient of variations (*COV*) of the spiral pipe ($N = 1$, $L = 1D$, $H = 3/8R$, and $\theta = 20°$) at 40D–50D, 50D–60D, 60D–70D, 70D–80D, and 80D–90D were lower than that of a straight pipe by about 3.908%, 2.825%, 1.289%, 0.186%, and 0.859%.

Institutional Review Board Statement: Not applicable.

Data Availability Statement: The data are only available upon request due to privacy restrictions.

Conflicts of Interest: Author Jiajia Xiao was employed by the company Jiangxi Zengxin Technology Co., Ltd. The remaining authors declare that the research was conducted in the absence of any commercial or financial relationships that could be construed as a potential conflict of interest.

References

1. Plumed-Ferrer, C.; von Wright, A. Fermented pig liquid feed: Nutritional, safety and regulatory aspects. *J. Appl. Microbiol.* **2009**, *106*, 351–368. [CrossRef] [PubMed]
2. Nannen, C.; Schmitt-Pauksztat, G.; Buscher, W.J.L. Microscopic test of dust particles in pig fattening houses: Differences between dry and liquid feeding. *Landtechnik* **2005**, *60*, 218–219.
3. Torok, V.A.; Luyckx, K.; Lapidge, S. Human food waste to animal feed: Opportunities and challenges. *Anim. Prod. Sci.* **2022**, *62*, 1129–1139. [CrossRef]
4. Kil, D.Y.; Stein, H.H. Board Invited Review: Management and feeding strategies to ameliorate the impact of removing antibiotic growth promoters from diets fed to weanling pigs. *Can. J. Anim. Sci.* **2010**, *90*, 447–460. [CrossRef]
5. Canibe, N.; Jensen, B.B. Fermented liquid feed-Microbial and nutritional aspects and impact on enteric diseases in pigs. *Anim. Feed. Sci. Technol.* **2012**, *173*, 17–40. [CrossRef]
6. Kobek-Kjeldager, C.; Vodolazs'ka, D.y.; Lauridsen, C.; Canibe, N.; Pedersen, L.J. Impact of supplemental liquid feed pre-weaning and piglet weaning age on feed intake post-weaning. *Livest. Sci.* **2021**, *252*, 252. [CrossRef]

7.   Xin, H.; Wang, M.; Xia, Z.; Yu, B.; He, J.; Yu, J.; Mao, X.; Huang, Z.; Luo, Y.; Luo, J.; et al. Fermented Diet Liquid Feeding Improves Growth Performance and Intestinal Function of Pigs. *Animals* **2021**, *11*, 1452. [CrossRef]

8.   Cullen, J.T.; Lawlor, P.G.; Cormican, P.; Gardiner, G.E. Microbial Quality of Liquid Feed for Pigs and Its Impact on the Porcine Gut Microbiome. *Animals* **2021**, *11*, 2983. [CrossRef]

9.   Zhao, D.; Guan, Y.; Qi, Z.; Wu, L.; Liang, L.; Yao, Y. Design and experiment of intelligent feeding vehicle for pig liquid feed. *J. Chin. Agric. Mech.* **2022**, *043*, 91–98. [CrossRef]

10.   Newitt, D.M.; Richardson, J.F.; Abbott, M.; Turtle, R.B. Hydraulic conveying of solids in horizontal pipes. *Trans. Inst. Chem. Eng.* **1955**, *33*, 93–113.

11.   Thomas, D.G. Transport characteristics of suspensions: Part VI. Minimum transport velocity for large particle size suspensions in round horizontal pipes. *AIChE J.* **2010**, *8*, 373–378. [CrossRef]

12.   Wood, R.J.K.; Jones, T.F.; Miles, N.J.; Ganeshalingam, J. Upstream swirl-induction for reduction of erosion damage from slurries in pipeline bends. *Wear* **2001**, *250*, 770–778. [CrossRef]

13.   Chen, J.; Wang, Y.; Li, X.; He, R.; Han, S.; Chen, Y. Erosion prediction of liquid-particle two-phase flow in pipeline elbows via CFD-DEM coupling method. *Powder Technol. Int. J. Sci. Technol. Wet Dry Part. Syst.* **2015**, *275*, 182–187.

14.   Durand, R. Basic relationships of the transportation of solids in pipes-experimental research. In Proceedings of the IAHR 5th Congress, Minneapolis, MN, USA, 1–4 September 1953; pp. 89–103.

15.   Yanuar, Y.; Gunawan, G.; Sapjah, D. Characteristics of Silica Slurry Flow in a Spiral Pipe. *Int. J. Technol.* **2015**, *6*, 916. [CrossRef]

16.   Watanabe, K.; Kamoshida, T.; Kato, H. Pressure loss of fly ash slurries in a spiral tube. *Trans. Jpn. Soc. Mech. Eng. Ser. B* **1988**, *54*, 1064–1072. [CrossRef]

17.   Qi, J.; Yin, J.; Yan, F.; Liu, P.; Wang, T.; Chen, C. Liquid–solid flow characteristics in vertical swirling hydraulic transportation with tangential jet inlet. *J. Mar. Sci. Eng.* **2021**, *9*, 1091. [CrossRef]

18.   Krishna, R.; Kumar, N.; Gupta, P.K. CFD investigation of pressure drop reduction in hydrotransport of multisized zinc tailings slurry through horizontal pipes. *Int. J. Hydrog. Energy* **2023**, *48*, 16435–16444. [CrossRef]

19.   Tang, J.; Gao, R. Numerical simulation of high-speed spiral flow in lifting pipe. *J. Jiangxi Univ. Sci. Technol.* **2015**, *36*, 64–68. [CrossRef]

20.   Yanuar, Y.; Waskito, K.T.; Mau, S.; Wulandari, W.; Sari, S.P. Helical Twisted Effect of Spiral Pipe in Generating Swirl Flow for Coal Slurries Conveyance. *J. Teknol.* **2017**, *79*, 69–79. [CrossRef]

21.   Charles, M.E.; Cheh, H.-S.; Chu, H.-L. The flow of "settling" slurries in tubes with internal spiral ribs. *Can. J. Chem. Eng.* **2009**, *49*, 737–741. [CrossRef]

22.   Li, H.; Tomita, Y. Characteristics of Swirling Flow in a Circular Pipe. *J. Fluids Eng.* **1994**, *116*, 370–373. [CrossRef]

23.   Fokeer, S.; Lowndes, I.S.; Hargreaves, D.M. Numerical modelling of swirl flow induced by a three-lobed helical pipe. *Chem. Eng. Process. Process Intensif.* **2010**, *49*, 536–546. [CrossRef]

24.   Zhou, J.-w.; Du, C.-l.; Liu, S.-y.; Liu, Y. Comparison of three types of swirling generators in coarse particle pneumatic conveying using CFD-DEM simulation. *Powder Technol.* **2016**, *301*, 1309–1320. [CrossRef]

25.   Ariyaratne, C. Design and Optimisation of Swirl Pipes and Transition Geometries for Slurry Transport. Ph.D. Thesis, University of Nottingham, Nottingham, UK, 2005.

26.   Rao, Y.; Liu, Z.; Wang, S.; Li, L.; Sun, Q. Numerical Simulation of Swirl Flow Characteristics of CO_2 Hydrate Slurry by Short Twisted Band. *Entropy* **2021**, *23*, 913. [CrossRef] [PubMed]

27.   Schaan, J.; Sumner, R.J.; Gillies, R.G.; Shook, C.A. The effect of particle shape on pipeline friction for Newtonian slurries of fine particles. *Can. J. Chem. Eng.* **2000**, *78*, 717–725. [CrossRef]

28.   Zhou, M.; Wang, S.; Kuang, S.; Luo, K.; Fan, J.; Yu, A. CFD-DEM modelling of hydraulic conveying of solid particles in a vertical pipe. *Powder Technol.* **2019**, *354*, 893–905. [CrossRef]

29.   Li, M.-z.; He, Y.-p.; Liu, Y.-d.; Huang, C. Pressure drop model of high-concentration graded particle transport in pipelines. *Ocean. Eng.* **2018**, *163*, 630–640. [CrossRef]

30.   Wu, J.; Wang, C.; Wang, M.; Liu, Y.; Li, Y. Numerical simulation of turbulent fluid flow and heat transfer in a circular tube with twisted tape inserts. *J. Zhengzhou Univ. (Eng. Sci.)* **2017**, *38*, 10–14. [CrossRef]

31.   Liang, J.; Rao, Y.; Wang, S.; Yan, S.; Ge, H.; Cai, Y. Numerical simulation of spiral flow and heat transfer in natural gas hydrate pipelines. *Oil-Gas Field Surf. Eng.* **2018**, *37*, 6–11. [CrossRef]

32.   Wen, C.; Cao, X.; Yang, Y. Swirling flow of natural gas in supersonic separators. *Chem. Eng. Process. Process Intensif.* **2011**, *50*, 644–649. [CrossRef]

33.   Yuan, F.; Wang, H.; Zhou, P.; Xu, A.; He, D. Heat transfer performances of honeycomb regenerators with square or hexagon cell opening. *Appl. Therm. Eng.* **2017**, *125*, 790–798. [CrossRef]

34.   Tao, Y.B.; He, Y.-L. A review of phase change material and performance enhancement method for latent heat storage system. *Renew. Sustain. Energy Rev.* **2018**, *93*, 245–259. [CrossRef]

35.   Yakhot, V.; Orszag, S.A. Renormalization group analysis of turbulence. I. Basic theory. *J. Sci. Comput.* **1986**, *1*, 3–51. [CrossRef]

36.   Zhang, J.; Xie, J.; Li, Y. Influence analysis of 2D dimple concave non-smooth units' depth on drag-reduction performance. *J. Chin. Agric. Mech.* **2016**, *37*, 44–48. [CrossRef]

37.   Messa, G.V.; Malavasi, S. Computational investigations of solid–liquid particle interaction in a two-phase flow around a ducted obstruction. *J. Hydraul. Res.* **2011**, *49*, 840–841. [CrossRef]

38. Li, M.; Tao, L.; Yu, Z.; Yu, Q. Numerical investigation on cooling and heat transfer of supercritical CO_2 in horizontal spiral groove tubes. *J. Eng. Therm. Energy Power* **2021**, *36*, 51–59. [CrossRef]

39. Basavarajappa, M.; Draper, T.; Toth, P.; Ring, T.A.; Miskovic, S. Numerical and experimental investigation of single phase flow characteristics in stirred tanks using Rushton turbine and flotation impeller. *Miner. Eng.* **2015**, *83*, 156–167. [CrossRef]

40. Tsuo, Y.P.; Gidaspow, D. Computation of flow patterns in circulating fluidized beds. *AIChE J.* **1990**, *36*, 885–896. [CrossRef]

41. Chen, L.; Duan, Y.; Liu, M.; Pu, W.; Zhao, C. Numerical simulation of characteristics of coal-water slurry flow in the inlet section of a horizontal Pipe. *J. Southeast Univ. (Nat. Sci. Ed.)* **2010**, *40*, 402–408. [CrossRef]

42. An, J.; Huang, K. Simulation design of pipeline type device for microwave heating of solid materials. *J. Microw.* **2015**, *31*, 35–42. [CrossRef]